Lab on a Chip

Devices and applications at the micro- and nanoscale

Accepted Manuscript

This article can be cited before page numbers have been issued, to do this please use: G. Li, L. Wan, Y. Chen, X. Zhang, A. Tang and H. Yang, *Lab Chip*, 2025, DOI: 10.1039/D5LC00274E.

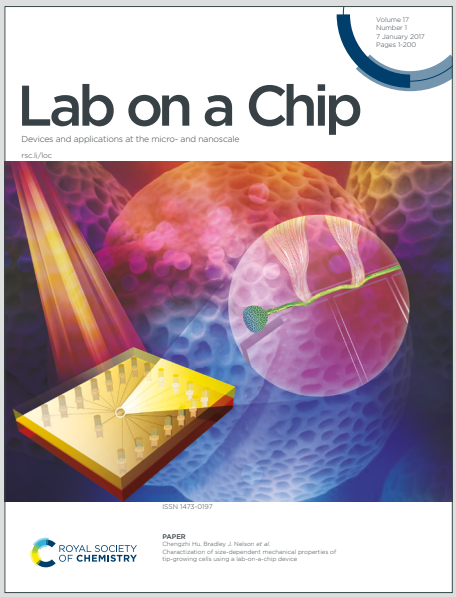

View Article Online
DOI: 10.1039/D5LC00274E

Size-selective sorting of kaolinite micro/nanoflakes *via* microfluidic filtration for wound hemostasis

Guangyao Li [‡ a], Liang Wan [‡ b], Ying Chen [*a], Xuming Zhang [*b], Aidong Tang [ac], Huaming Yang [*ad]

[a] Engineering Research Center of Nano-Geomaterials of Ministry of Education, Laboratory of Advanced Mineral Materials, Faculty of Materials Science and Chemistry, China University of Geosciences, Wuhan 430074, China

[b] Department of Applied Physics & Research Centre for Resources Engineering towards Carbon Neutrality (RCRE), The Hong Kong Polytechnic University, Hong Kong, 999077, China

[c] College of Chemistry and Chemical Engineering, Central South University, Changsha 410083, China

[d] Hunan Key Laboratory of Mineral Materials and Application, School of Minerals Processing and Bioengineering, Central South University, Changsha 410083, China

[‡] These authors contributed equally to this work.

[*] Corresponding author

E-mail: chenying2021@cug.edu.cn; xuming.zhang@polyu.edu.hk ; hm.yang@cug.edu.cn

View Article Online
DOI: 10.1039/D5LC00274E

Abstract

Kaolinite, a natural micro/nano clay material, exhibits remarkable effect on wound hemostasis, yet its efficacy is critically limited by heterogeneous particle sizes. Therefore, sorting based on size differences is essential to improve its performance. However, kaolinite with layer structure presents challenges in sorting compared to spherical or elliptical materials, and the size distribution ranges continuously from nanometers to micrometers, which poses significant challenges for precise sorting. Hence, we developed a dual-layer microfluidic filtration chip, to enable high-throughput sorting of kaolinite micro/nanoflakes (size from 1.582 to 0.377 μm). The dual-layer filter membrane structure with graded pore sizes enabled selective sorting of kaolinite particles within a specific size range, and the co-flow fluid arrangement was employed to alleviate membrane clogging. The hemostatic properties of kaolinite particles with different sizes were evaluated through *in-vivo* and *in-vitro* experiments, revealing the significant size-dependent effects of kaolinite on wound hemostasis. The mechanism of different sizes of kaolinite in the process of coagulation, especially the effect on platelet activation and coagulation factor activation, provided theoretical basis for optimizing kaolinite-based hemostatic materials. This work established a scalable microfluidic strategy for precise sorting of sheet nanomaterials and improved the translational potential of kaolinite in emergency wound hemostasis.

KEYWORDS: *Microfluidic filtration*, *kaolinite micro/nano-flakes sorting*, *size effect*, *wound hemostasis*

View Article Online
DOI: 10.1039/D5LC00274E

Introduction

Biomedicine is crucial to human health and has long been a focal point of international research.[1] Within this domain, hemostatic materials are indispensable for controlling bleeding and saving lives, especially in emergency situations such as battlefields, traffic accidents, and other traumatic injuries.[2] Natural mineral materials, including zeolite, montmorillonite, and kaolinite, possess well-developed microporous structures, large specific surface areas, and exceptional adsorption capabilities. These intrinsic properties facilitate the rapid absorption of wound exudates and enhance blood coagulation processes, leading to effective hemostatic control. Furthermore, their widespread natural occurrence and cost-effectiveness render them particularly suitable for extensive practical applications.[3-5] Although zeolite and montmorillonite show significant potential for hemostatic applications, their clinical implementation is limited by several critical factors that require careful consideration.[6-9] Specially, zeolite's macroporous structure may cause excessive platelet activation and thrombosis risks,[10] while montmorillonite's strong adsorption can form occlusive barriers that delay hemostasis and its slow biodegradation may impair wound healing,[11] these limitations restrict their clinical translation despite their inherent potential.

Kaolinite, as a natural clay mineral with the molecular formula $Al_2Si_2O_5(OH)_4 \cdot nH_2O$ (n=0 or 2), has emerged as a superior candidate for next-generation hemostatic materials, distinguished by its exceptional safety profile and therapeutic efficacy.[3, 12] The unique microporous architecture and optimal adsorption characteristics of kaolinite facilitate efficient wound exudate management and promote physiological platelet aggregation and activation, thereby establishing an ideal microenvironment to accelerate coagulation cascade initiation.[13] Unlike other mineral-based hemostats, kaolinite demonstrates remarkable biocompatibility and negligible immunogenicity, which significantly mitigate inflammatory responses and preserves tissue integrity during the healing process.[14] Furthermore, kaolinite exhibits rapid clearance kinetics from the wound microenvironment, mitigating the potential for foreign body reactions while creating favorable conditions for physiological wound

View Article Online
DOI: 10.1039/D5LC00274E

healing progression. Despite its inherent advantages, natural kaolinite is fundamentally constrained by its morphological characteristics, particularly its large particle dimensions and heterogeneous size distribution, which critically undermine its hemostatic performance.[15, 16] Specifically, the larger particle size hinders the rapid penetration of kaolinite particles to the depths of the wound, thereby restricting their full contact with blood. Moreover, the non-uniform adsorption layer formed by unevenly sized particles on the wound surface fails to effectively facilitate the uniform aggregation and activation of platelets, consequently compromising the speed and quality of blood coagulation.[17-19] This morphological irregularity thus leads to inconsistent thrombin generation and fibrin network formation, ultimately manifesting as compromised coagulation kinetics and suboptimal clot stability.[20] These limitations result in a suboptimal hemostatic efficiency of natural kaolinite, rendering it inadequate to meet the stringent demands of emergency hemostasis.

Currently, the size control and sorting of kaolinite have attracted widespread attention and have been the subject of extensive research. In terms of size control, common methods include mechanical grinding[21], chemical modification[22], heat treatment[23], solvothermal method[24], ultrasonic treatment[25], and electrostatic deposition[26]. For the sorting and collection of kaolinite, a variety of technical means are also available, such as sieving, sedimentation, ultrasonic dispersion and classification, air classification, magnetic separation, etc.[27, 28] In recent studies, separation techniques for layered materials have achieved significant progress. For example, Zhao *et al.* reviewed the latest advances in selective separation and precise control of two-dimensional (2D) layered membranes, discussing the effects of size exclusion, charge properties, and chemical affinity on the accurate separation of 2D membranes, along with a summary and analysis of existing research on their precise control and selective separation processes.[29] Additionally, Zhang *et al.* enhanced separation accuracy by hybridizing materials of different dimensions to regulate the structure and performance of layered membranes.[30] However, current techniques for kaolinite size sorting are plagued by several critical limitations. These methods mainly rely on time-consuming multi-step processes under batch conditions, which are

View Article Online
DOI: 10.1039/D5LC00274E

inherently inefficient for particle sorting. Although effective for coarse particles (>75 μm), they lack extensibility and accuracy in micro/nano-scale applications. Consequently, the development of a precise, scalable, and environmentally sustainable approach for kaolinite size sorting remains an unresolved scientific and technological challenge.

Microfluidics, characterized by its microscale operation, high-precision control and high-throughput processing, has shown significant advantages in material screening.[31-33] For example, microfluidic filtration technology has important applications in cell sorting. Kim *et al.* utilized microfluidic filtration technology to achieve the separation of white blood cells from whole blood with a purity greater than 90%[34], and Qiu *et al.* filtered large tissue fragments and collected single cells.[35] Therefore, microfluidic filtration chips are expected to enable the sorting of kaolinite particles at micro/nano-scale sizes. In this context, microfluidic sorting technology provided inspiration for the separation of layered materials. However, current microfluidic sorting techniques (e.g., Deterministic Lateral Displacement (DLD), inertial microfluidics), while effective for spherical particles, faced limitations when processing layered materials due to their geometric characteristics (high aspect ratio, continuous size distribution). For instance, Liu *et al.* attempted to use inertial flow to separate two fine mineral particles, but the purity of separation needed to be improved.[36] Therefore, there is an urgent need to develop novel microfluidic strategies for the sorting of kaolinite particles to address challenges related to clogging, throughput, and resolution.

In this work, a unique microfluidic filter was designed and achieved precise sorting of kaolinite micro/nanoflakes after pre-treatment by intercalation and ultrasonic exfoliation. The device integrated traditional filtration and tangential flow filtration modes, utilizing co-flow to alleviate membrane clogging, which was expected to enable the sorting and collection of micro/nano-sized kaolinite from a mixture of particles with a continuous size distribution. Meanwhile, the hemostatic performance of kaolinite particles with varying sizes was systematically evaluated through both *in-vivo* and *in-vitro* experiments, uncovering the significant size-dependent effects of kaolinite on

View Article Online
DOI: 10.1039/D5LC00274E

wound hemostasis. This study provided an effective and controllable method for high-precision screening of micro/nano-scale kaolinite, which not only improved the hemostatic performance, but also enhanced the practicality and social value of microfluidics.

Results and discussion

Screening of kaolinite particles based on microfluidics

The microfluidic filtration device was developed and used for size-based sorting of kaolinite particles after pre-treatment (**Fig. 1a**). The microfluidic filtration chip was constructed using a multilayer assembly approach, as the cross-sectional details provided in **Fig. 1b**. The microfluidic filtration chip had a total of 7 layers, which were the upper and lower sealing layers. In the middle, there were 3 layers of laser-processed polymethyl methacrylate (PMMA) plates as the upper, middle and lower flow channel layers. The flow channel layers were separated by elastomeric silicone gaskets and polycarbonate filter membranes respectively. The polycarbonate filter membrane had the advantage of being low in price and could be cut at will. The entire chip was finally fixed by screw. Compared with fixing glue, this method was easy to disassemble and facilitated replacement of the filter membrane at any time. The microfluidic chip (7.5 cm×4.5 cm×1 cm) featured a serpentine channel design (PMMA/gasket thickness: 1 mm, channel width: 1 mm) to prolong particle residence time near the filtration membrane. This device integrated a filtration mechanism combining conventional filtration with tangential flow filtration (TFF) technology (**Fig. 1c**), which offered the following advantages for the separation of layered materials: (1) Reduced clogging; Layered materials tended to form dense stacks or align parallel to the membrane surface in conventional filtration, causing rapid clogging. TFF introduced tangential shear forces that disrupted this stacking. (2) Size selectivity; The tangential flow enhanced the separation of layer kaolinite from thicker aggregates by exerting differential shear forces, in that thinner flakes remained suspended in the flow while thicker particles were retained, which was critical for obtaining monodisperse 2D materials.

View Article Online
DOI: 10.1039/D5LC00274E

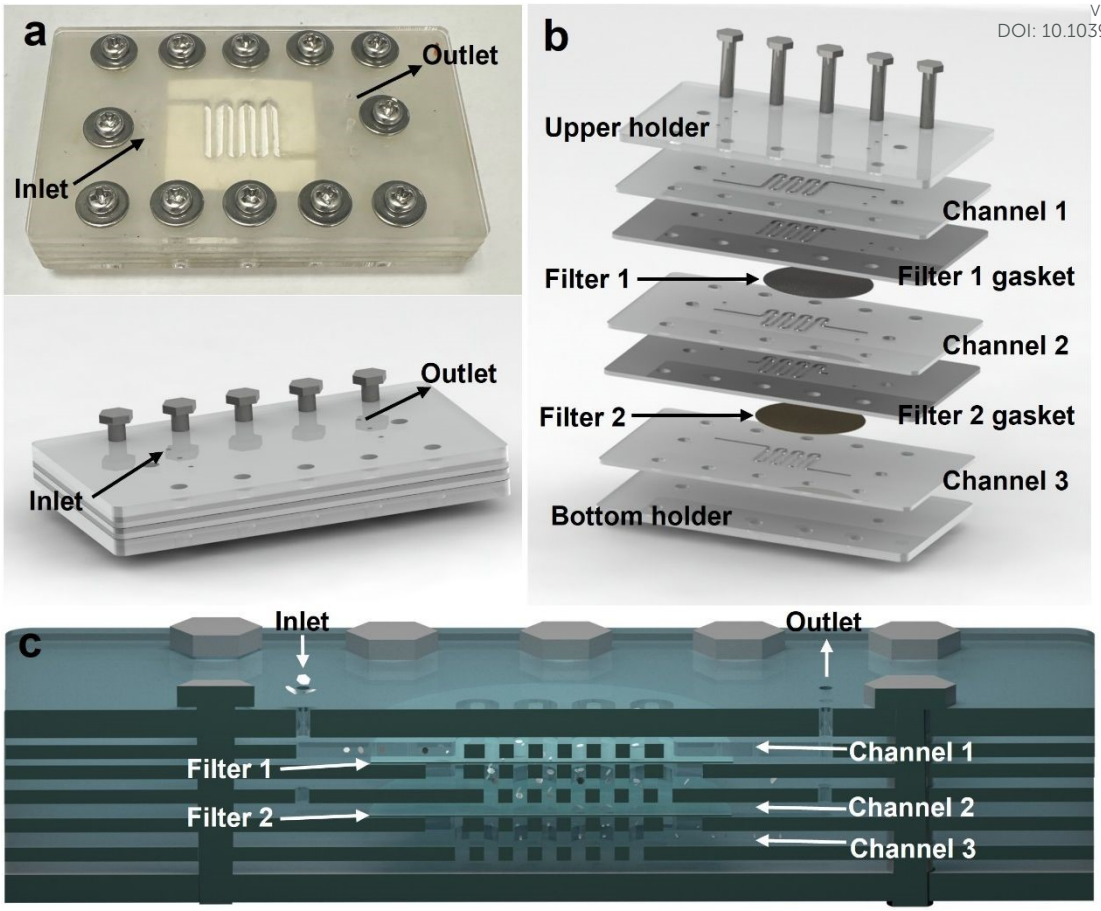

Fig. 1 (a) Physical prototype (up) and model diagram (down) of microfluidic filter device. (b) Internal structural details and (c) cross-sectional details including three channel layers, two gasket layers with filters, and two layers to seal the top and bottom of the device.

The schematic illustration and physical image of the microfluidic filtration device for the screening of kaolinite micro/nano-flakes was illustrated in **Fig. 2a** and **Fig. S1**. The system integrated customizable polycarbonate membranes and utilized four precision pumps: an injection pump (200 μL/min) for sample introduction (defined as Kaol-0), and three withdrawal pumps (Outlet 1: 40 μL/min for Filter 1 particle removal; Outlets 2 and 3: 40 μL/min and 120 μL/min respectively) enabling size-based separation through sequential filtration. The sample was directed through microfluidic channels to contact membrane filter 1 (0.8 μm), which featured larger pore dimensions. Particles permeating through this membrane subsequently entered the intermediate channel where they encountered the membrane filter 2 (0.45 μm) with significantly reduced pore sizes. Particulate matter smaller than the membrane's pore specifications migrated to the bottom channel and ultimately exit through the outlet port. A proportion

of the sample could alternatively be guided along the membrane surfaces and discharged through the co-flow outlet. Three dedicated outlet pumps (defined as Outlet 1, 2 and 3) were strategically positioned to withdraw the kaolinite suspension from the microfluidic chip, thereby precisely regulating the hydrodynamic pathways and flow distribution within the system.

The morphologies of kaolinite at different Outlet (1, 2 and 3) were observed by optical microscopy (**Fig. 2b-d**), and the results showed that kaolinite particles with different sizes were collected at Outlet 1, 2 and 3, respectively, indicating that the dual-layer microfluidic filtration chip effectively sorted according to particle size. Compared to the unused membrane, the membrane surface exhibited severe clogging when kaolinite was sorted using a direct filtration method (**Fig. S2a-b**). However, the dual-layer microfluidic filtration chip designed in this work, which employed the co-flow fluid arrangement, exhibited uniform membrane surface after kaolinite sorting, effectively alleviating the clogging issue (**Fig. S2c**). This design not only improved the efficiency of material sorting but also extended the service life of the membrane, thereby demonstrating significant advantages in practical applications.

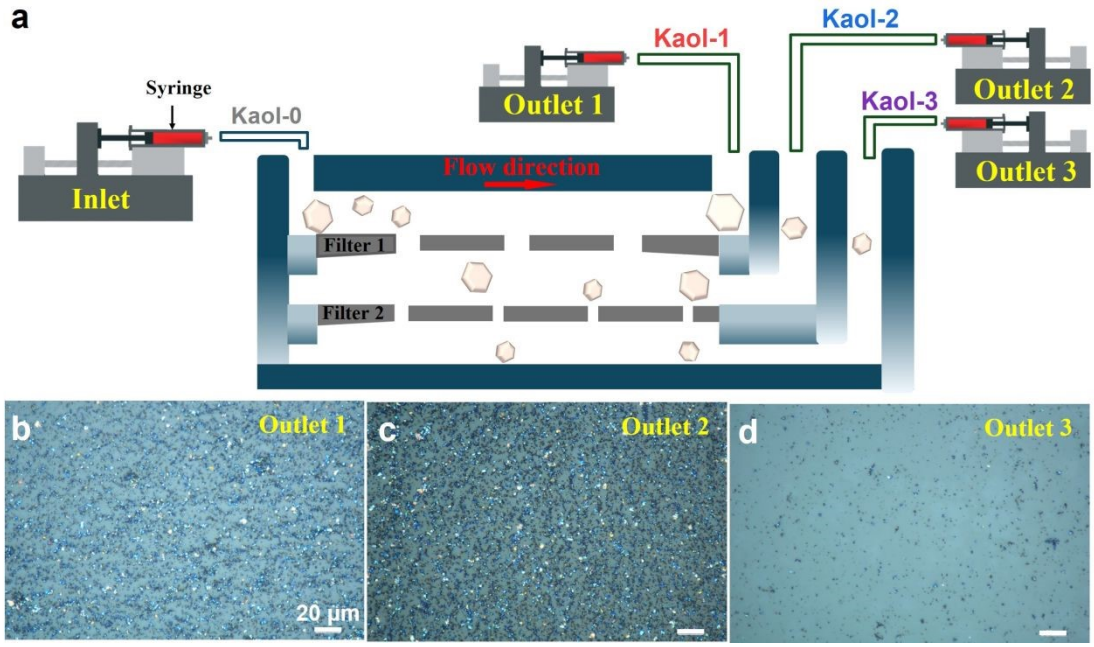

Fig. 2 (a) Schematic illustration of the microfluidic filtration device for the screening of micro/nano-scale kaolinite. (b-d) Optical microscope view of the collection at Outlet 1, 2, and 3 respectively.

View Article Online
DOI: 10.1039/D5LC00274E

Structural characteristics of kaolinite with different sizes

The particle size distribution of kaolinites screened from Outlet 1, 2 and 3 were measured by Dynamic Light Scattering (DLS), respectively. By contrast, the size distribution range of unscreened kaolinite (Kaol-0) was wide, and the median diameter (D_{50}) reached 2.7±0.537 μm, indicating that the size of Kaol-0 was large and uneven (**Fig. S3**). After two-step intercalation, ultrasonic exfoliation intercalation and chips screening, the overall particle size distribution of kaolinite shifted to lower particle size and the peak shape was narrower, indicating that the microfluidic chips realized the sorting and collection of kaolinite of different sizes, in which the median particle size (D_{50}) of Kaol-1, Kaol-2 and Kaol-3 were 1.582±0.127, 0.617±0.033 and 0.377±0.009 μm, respectively (**Fig. 3a-b**). The morphology of kaolinite was characterized by scanning electron microscopy (SEM) and transmission electron microscopy (TEM), respectively. The SEM results indicated that the kaolinite maintained lamellar structure before and after screening (**Fig. 3c** and **Fig. S4**). It was clearly observed that the lamellar structure of Kaol-0 was not uniform in size. After two-step intercalation, ultrasonic exfoliation intercalation and chips screening, the morphology of lamellar kaolinite was more regular, and the average diameter of Kaol-1, 2 and 3 were 1.250±0.035, 0.575±0.012 and 0.328±0.004 μm respectively, which was basically consistent with the particle size distribution results. The lamellar hexagonal morphology of kaolinite was obviously observed by TEM (**Fig. S5**). The stack of Kaol-0 was tighter, and the edges were regular and neat. However, with the decrease of particle size, the lamellar kaolinite was disorganized, and the exposed edges were passivated and damaged. Since the input kaolinite particles exhibited continuous size distribution, the sorted kaolinite collected from each outlet possessed a specific size range. The purity of kaolinite collected from Outlet 1, 2, and 3 reached 99.5%, 98.5%, and 100% respectively. After sorting, the recovery rate of kaolinite achieved 83.4%, 60.1%, and 56.1%, respectively. These results demonstrated the performance of microfluidic filtration chip in fractionating kaolinite with high size selectivity.

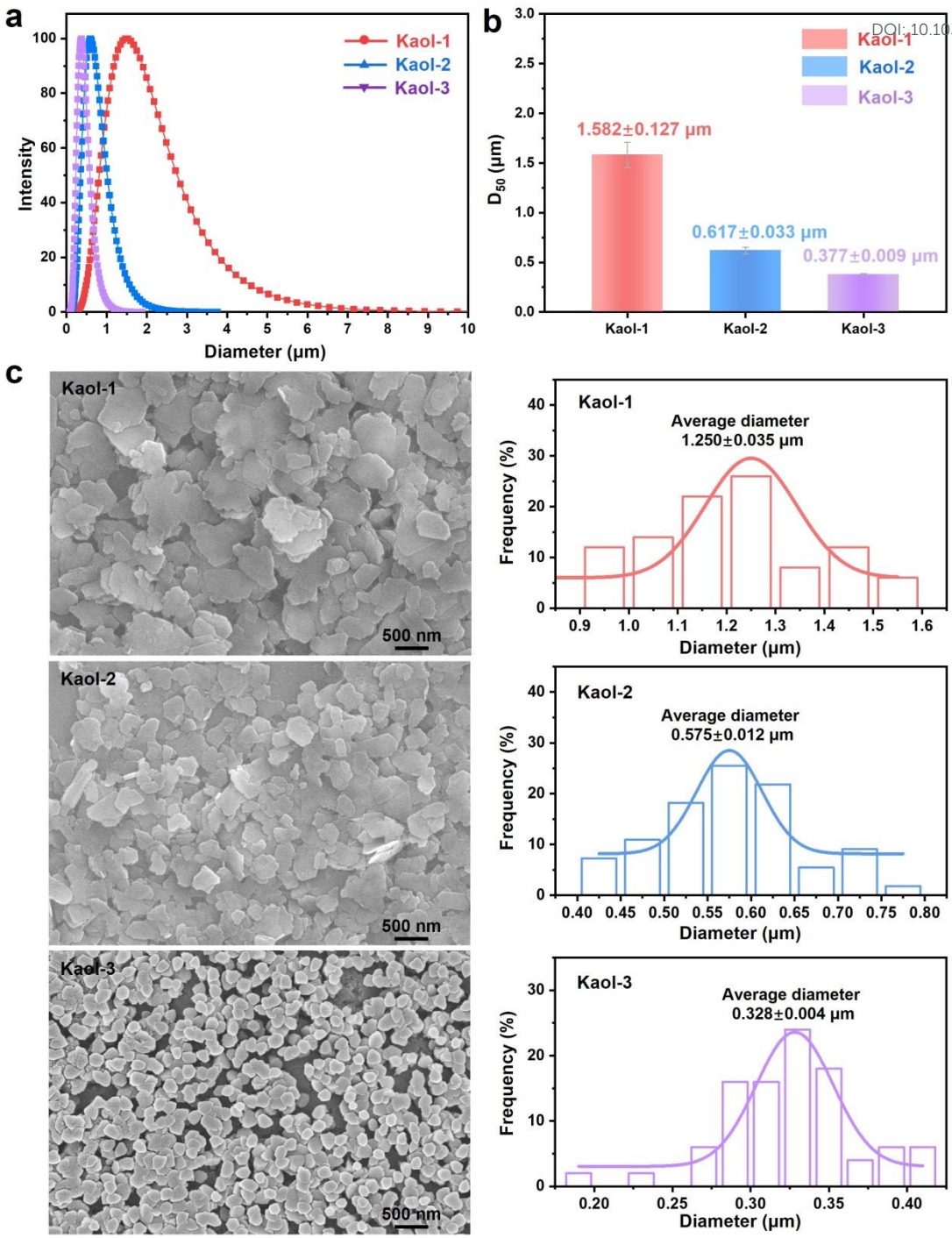

Fig. 3 (a) Particle size distribution and (b) median particle size (D_{50}). (c) SEM images and particle size statistical histogram.

The phase structure of kaolinite with different sizes was characterized by X-Ray Diffraction (XRD), as shown in **Fig. 4a**. The characteristic diffraction peaks of Kaol-0 at (001) and (002) were sharp and strong, indicating that the crystalline structure of unscreened kaolinite was regular and complete. With the decrease of the size, especially in Kaol-3, the diffraction peak intensity corresponding to the (001) crystal surface of

View Article Online
DOI: 10.1039/D5LC00274E

kaolinite decreased gradually, and the diffraction peak widened obviously, indicating that the layer structure of kaolinite was destroyed, and the order degree was reduced. However, the position of (001) and (002) diffraction peaks were not shifting significantly, indicating that the process of ultrasonic exfoliation only changed the stacking degree of kaolinite in the *c*-axis, and did not damage the *a*- and *b*-axis lamellar structure of kaolinite.

Brunauer-Emmett-Teller (BET) analysis was performed to compare the difference of specific surface area and pore structure of kaolinite with different sizes. As shown in **Fig. 4b**, Kaol-0, 1, 2 and 3 had similar N_2 adsorption and desorption isotherms, all belonging to type VI adsorption isotherms. The specific surface area and pore structure parameters were exhibited in **Fig. 4c** and **Table S1**. The specific surface area and pore structure of Kaol-0 were generally low. With the decrease of kaolinite particle size, the specific surface area and pore structure of kaolinite was expanded, among which Kaol-3 reached the surface area of 34.213 m^2g^{-1}, the pore size of 24.838 nm, and the pore volume of 0.242 cm^3g^{-1}, respectively. These results were due to the loose accumulation caused by the reduction of kaolinite size, resulting in the increase of mesoporous and pore size of kaolinite.

In the process of hemostasis, the electronegativity of hemostatic materials is the key to affecting the hemostatic effect. The aluminosilicate layered structure in Kaolinite is composed of silicon-oxygen tetrahedral layers (Si-O) and aluminum-oxygen octahedral layers (Al-O). Accompanied by the isomorphic substitution of Al for Si, it led to the generation of permanent negative charges on the crystal planes of kaolinite. Simultaneously, the surface of kaolinite contains abundant active groups such as Al-O, Si-O, and Al-OH, which readily undergo deprotonation in aqueous solutions, thereby further increasing the surface negativity. As the particle size of kaolinite decreases, its specific surface area increases significantly, which means that per unit mass of kaolinite possesses more surface active sites capable of adsorbing additional negative charges, consequently enhancing its electronegativity. Furthermore, the reduced particle size leads to more concentrated charge distribution on the particle surfaces, which further amplifies the overall electronegativity. The Zeta potential (using deionized water,

pH=6.8) analysis results indicated that kaolinite always maintained obvious electronegativity with the decrease of size, and the smaller the kaolinite particles, the stronger the electronegativity (**Fig. 4d**). Negative charge is benefited to facilitate the self-activation pathway to trigger the intrinsic clotting cascade, thus promoting hemostasis. **Fig. S6** exhibited the zeta potential of kaolinite under simulated physiological conditions (using PBS buffer, pH 7.4). These results indicated that the electronegativity of kaolinite increased further due to enhanced deprotonation at higher pH, leading to higher negative charge density.

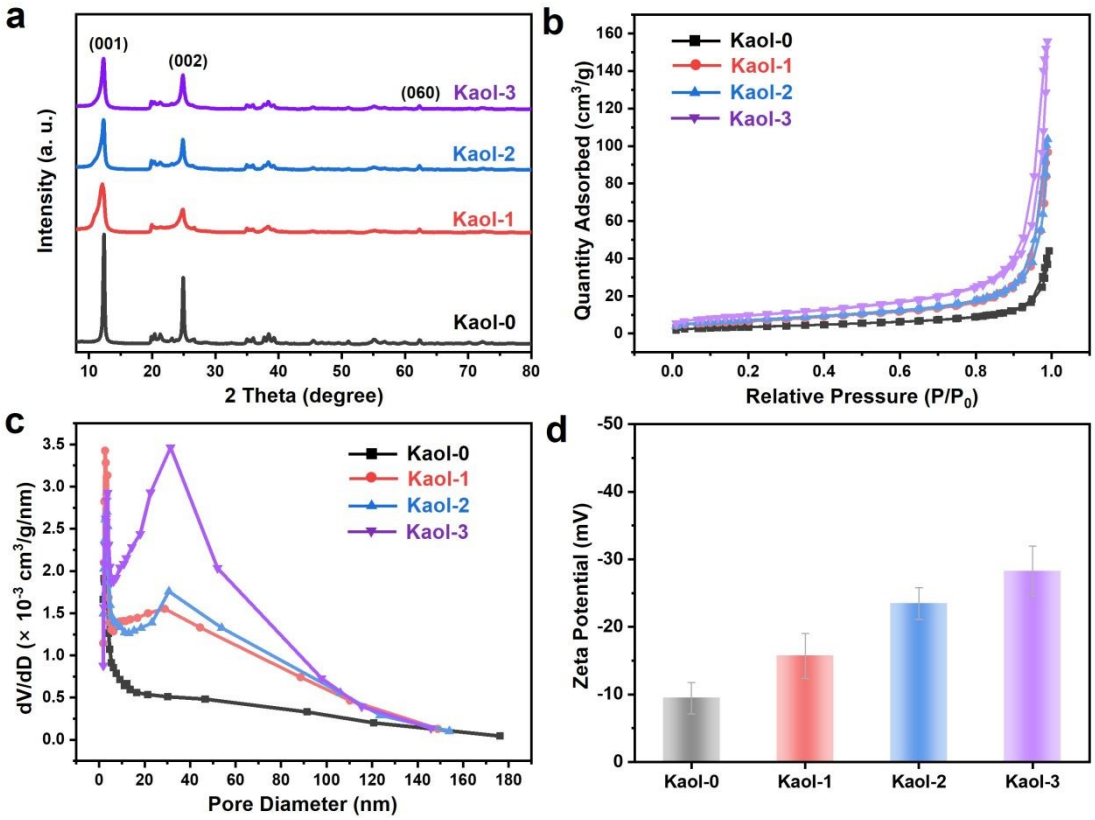

Fig. 4 (a) XRD patterns, (b) Nitrogen adsorption/desorption isotherms, (c) BJH pore size distribution and (d) zeta potential (pH=6.8) of Kaol-0, 1, 2 and 3, respectively.

Hemostatic performance evaluation

The *in-vitro* hemostatic effect of kaolinite was evaluated through dynamic coagulation experiment, and the experimental process and details were shown in **Fig. 5a** and **Fig. S7**. **Fig. S7** illustrated three key steps of the dynamic coagulation assay: (Ⅰ) setup of blank/control/experimental groups, (Ⅱ) co-incubation of blood with samples, and (Ⅲ) dissolution of uncoagulated red blood cells to quantify hemostatic

View Article Online
DOI: 10.1039/D5LC00274E

efficacy. Specifically, 10 mg of sample was mixed with 100 μL rabbit blood, followed by the addition of 10 μL 0.2 M $CaCl_2$ to initiate coagulation. After 10 min of incubation at 37 °C, the reaction was terminated with deionized water, and absorbance at 540 nm was measured post-centrifugation. The hemostatic effect of kaolinite with different sizes was evaluated by measuring the absorbance of hemoglobin released from unbound red blood cells. As shown in **Fig. 5a** inset, the absorbance of kaolinite samples was significantly reduced, indicating the coagulation effect of kaolinite was obvious. Moreover, as the size of kaolinite decreased, the absorbance decreased further, which proved that the hemostatic performance of kaolinite was dependent on the size.

Blood clotting index (BCI) further reflected the clotting ability of the samples to the blood, in which the higher the BCI value, the slower the clotting rate. As shown in **Fig. 5b**, the BCI value of Kaol-3 reached 24.69%, further confirmed that the hemostatic advantage in small size kaolinite. The whole blood clotting time of kaolinite was exhibited in **Fig. 5c**, which was nearly half shorter than that of the Control group. The clotting time of kaolinite was shortened by more than 50%, among which Kaol-3 could reach less than 50 s.

By observing the adhesion of red blood cells on the surface of materials, the hemostatic performance of the materials can be evaluated. Under the view of SEM, the red blood cells exhibited a typical biconcave disc shape (**Fig. S8**). **Fig. S9** showed the interaction between kaolinite and red blood cells, where pronounced aggregation and stacking between kaolinite particles and red blood cells were observed, which was attributed to the interplay between the surface properties of kaolinite and the red blood cell membrane. Under the view of well-dispersed conditions, kaolinite particles were found to adhere tightly to the red blood cell surface (**Fig. 5d**). Additionally, variations in kaolinite particle size led to differences in red blood cell surface coverage and distribution. Morphology of adherent red blood cells indicated that smaller kaolinite particles were more conducive to adhesion with red blood cells. The layer structure and mesoporous structure of kaolinite could absorb blood plasma, reduce blood fluidity, and facilitate the adhesion and aggregation of red blood cells on its surface. This process promoted the activation of the intrinsic coagulation cascade, thereby achieving

View Article Online
DOI: 10.1039/D5LC00274E

hemostasis, which was supported by extensive literature reporting.[13, 37]

Subsequently, the mouse liver hemorrhage model was evaluated as the *in-vivo* hemostatic tests (**Fig. 5e** and **Fig. S10**). As shown in **Fig. 5f**, with the size of kaolinite decreasing, the liver blood loss in mice was reduced, with the blood loss potentially dropping to as low as 70 mg (Kaol-3). At the same time, the hemostasis time was also significantly reduced (**Fig. 5g**), with the hemostasis time between Kaol-0 and Kaol-3 differing by nearly twice, and that in Kaol-3 was only 72 s.

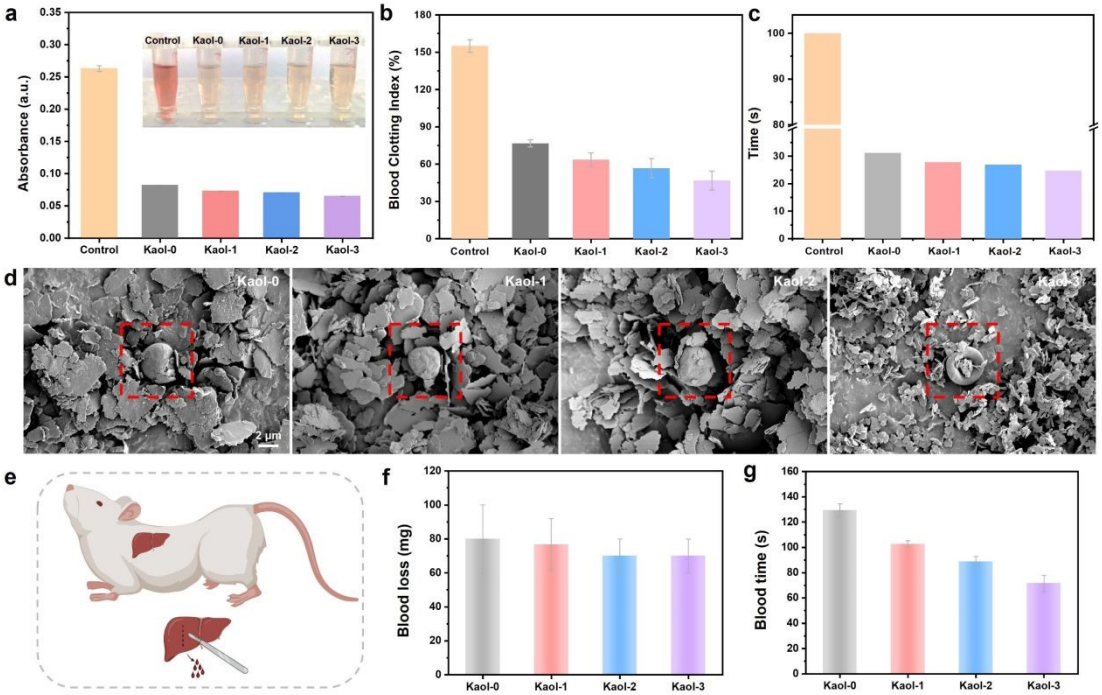

Fig. 5 (a) *In-vitro* hemostatic effect of samples evaluated through dynamic coagulation experiment. (b) Blood clotting index (BCI) and (c) hemostasis time of Kaol-0, 1, 2 and 3, respectively. (d) SEM images of interfacial interactions between samples and red blood cells (scale bar: 2 μm). (e) Schematic diagram of the mouse liver hemorrhage model. (f) Blood loss and (g) hemostasis time of different groups in the mouse liver hemorrhage model.

The coagulation function was evaluated by incubating kaolinite with platelet-poor plasma (PPP) suspension and measuring key parameters including activated partial thromboplastin time (APTT), prothrombin time (PT), thrombin time (TT), and fibrinogen (Fib) levels. These parameters respectively reflect the intrinsic and extrinsic coagulation pathways, fibrinogen conversion capacity, and plasma fibrinogen concentration, thereby providing valuable insights for clinical diagnosis and therapeutic interventions. As shown in **Fig. 6a**, all four measured parameters including APTT, PT,

View Article Online
DOI: 10.1039/D5LC00274E

TT and Fib remain within their respective normal reference ranges. A significant reduction of PT in Kaol-1, 2 and 3 groups respectively were observed compared to the Blank group, demonstrating that kaolinite exhibited a notable activation effect on the extrinsic coagulation pathway. The lack of significant changes in APTT and TT indicated that kaolinite primarily activated the extrinsic coagulation pathway, with minimal impact on intrinsic pathways. Furthermore, the decreased Fib level indicated that kaolinite had a certain adsorption effect on plasma proteins.

To investigate the interaction between kaolinite and platelets, kaolinite was co-incubated with platelet-rich plasma (PRP), simulating its effects on platelet activation and aggregation (**Fig. 6b**). Following FITC-phalloidin fluorescent staining, adherent platelets were specifically labeled, exhibiting distinct bright green fluorescence. The fluorescence intensity correlated positively with the number of adherent platelets, while the negative control group displayed no significant fluorescent signal. The presence of abundant negative charges and Si-OH functional groups on the kaolinite surface was found to promote robust platelet adhesion. Notably, a reduction in kaolinite particle size resulted in enhanced fluorescence intensity, demonstrating that kaolinite with a higher specific surface area exhibits superior platelet interaction capabilities.

The activation status of platelets was quantitatively evaluated using fluorescently labeled antibodies that specifically target granular membrane proteins (such as CD62P) expressed on the surface of activated platelets. Flow cytometric (FCM) analysis was performed to determine the platelet activation levels following kaolinite incubation (**Fig. 6c**). In the histogram of CD62P PE-A, with the particle size of kaolinite decreased and uniformity improved, the proportion of activated platelets gradually increased, indicating that the distinct size-dependent relationship in kaolinite-induced platelet activation. In the scatter plot of CD62P PE-A/CD61 FITC-A, the platelet activation ratio in Kaol-3 reached 6.36%, which was three times higher than that of the blank group (1.94%) and nearly twice that of Kaol-0 (3.38%) and Kaol-1 (3.60%), further confirming the hemostatic application advantages and size-dependent characteristics of kaolinite.

Kaolinite effectively adsorbs blood cells and platelets through its unique layered

structure and abundant surface hydroxyl groups, thereby promoting blood coagulation. Moreover, the smaller the size of kaolinite, the larger the specific surface area, and the greater the contact area with blood, which was more conducive to promoting hemostasis. The flaky structure and mesoporous structure of kaolinite could adsorb blood, reducing its fluidity, allowing red blood cells to adhere and aggregate on the surface, promoting the auto-activation to trigger the intrinsic coagulation cascade, thereby achieving hemostatic function. In conclusion, the synergistic effect between the size, morphology, mesoporous structure and surface negative charge of kaolinite is the key to its excellent hemostatic performance.

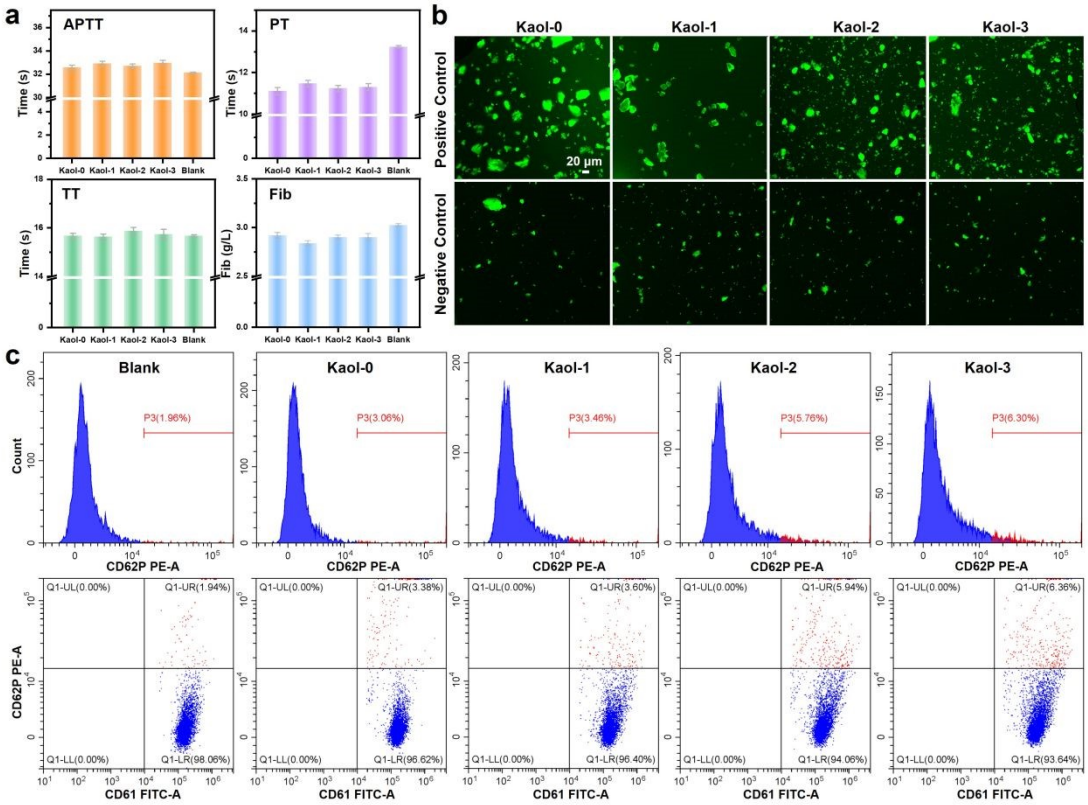

Fig. 6 (a) Results of clinical standard coagulation test. (b) The adherent platelets stained by FITC-Phalloidin. (c) FCM analysis diagram of platelet activation (CD61 + CD62p) of Kaol-0, 1, 2 and 3, respectively.

Conclusion

In this work, the dual-layer microfluidic filtration chip achieved high-throughput sorting of kaolinite micro/nanoflakes. This dual-layer filtration membrane structure with graded pore sizes allowed for selective sorting of kaolinite particles within a

View Article Online
DOI: 10.1039/D5LC00274E

specific size range, and the co-flow fluid arrangement effectively mitigated membrane clogging, enhancing the overall efficiency and reliability of the filtration process. The kaolinite particles with different sizes were further selected for subsequent structural characterization and hemostatic performance studies, and the experiments showed that small-size particles (Kaol-3) exhibited optimal hemostatic properties, which was attributed to its unique physical and chemical properties, including the abundant hydroxyl groups, two-dimensional layered structure, large specific surface area, and negative surface charge of kaolinite. Moreover, mechanism analysis revealed the smaller the size of the kaolinite, the more pronounced the size effect, which was more conducive to contact with blood, promote platelet aggregation and thus enhance hemostasis. This work not only provided a microfluidic technical solution for the high-throughput sorting of natural mineral materials but also laid a theoretical and technical foundation for the development of efficient hemostatic dressings.

View Article Online
DOI: 10.1039/D5LC00274E

Experimental section

Materials and reagents

Kaolinite (Pharmaceutical grade) was purchased from Shanghai Aladdin Biochemical Technology Co., LTD (Shanghai, China). $CaCl_2$, Dimethyl sulfoxide (DMSO) and Urea were procured from Sinopharm Chemical Reagent Co. Ltd (Shanghai, China). All reagents were used without further purification. Deionized water (DI, 18.2 $\Omega \cdot cm^{-1}$) was used throughout the experiments. The membranes used in this work were purchased from MemberSpace (USA), and the core parameters were exhibited in **Table S2**.

Kaolinite pre-treatment

The raw materials of kaolinite were firstly broken before the screening, which was realized by two-step intercalation and ultrasonic exfoliation. Typically, a 10 g kaolinite was added to the mixed solution of 90.0 mL DMSO and 10.0 mL DI water and stirred for 24 h at 60 °C. The suspension was centrifuged, and the precipitate was washed several times using deionized water, and the Kaolinite complex intercalated by DMSO (Kaol-DMSO) were obtained. Then, a 5 g Kaol-DMSO was added to the 50 mL saturated urea solution (13 mol/L) and stirred for 24 h at 60 °C. The suspension was centrifuged, and the precipitate was washed several times using deionized water, and the Kaolinite complex intercalated by urea (Kaol-Urea) were obtained. Finally, a 2 g Kaol-Urea was dispersed in 200 mL deionized water and ultrasonic exfoliation for 5 h at 60 °C with a power of 1500 W.

Characterization

X-ray diffraction (XRD) patterns were captured with a BRUKER D8 ADVANCE diffractometer, utilizing Cu Kα radiation at 40 kV/40 mA, scanning from 2θ of 5-80° at a rate of 5 °/min. The field-emission scanning electron microscopy (SEM) images were gotten from the Zeiss Supra 55 SEM. High-resolution transmission electron microscopy (HRTEM) images were obtained on a JEOL JEM-2010 transmission electron microscope. The Brunauer-Emmett-Teller (BET) surface area was collected by TriStar Ⅱ 3200. Surface area and porosity metrics were gauged using N_2-adsorption-desorption isotherms and analyzed via the BJH method. Zeta potential was

View Article Online
DOI: 10.1039/D5LC00274E

measured with a Nano Brook 90plus PALS analyzer. Contact angle determinations were made using Data physics OCA-20.

Dynamic coagulation effects

Firstly, weigh 10 mg samples and add them to 6-well plates and add 100 μL blood to each well, which was New Zealand white rabbits' blood and used in the following experiment referred to this type. Then immediately add 10 μL 0.2M $CaCl_2$ to trigger coagulation. The 6-well plates were incubated in a water bath at 37 ℃ for 10 min. Then add 10 mL of deionized water drop by drop to avoid damaging blood clots, which was used to stop the coagulation reaction. After that, 5 mL of the liquid was then removed and centrifuged at 1000 rpm for 1 min. The supernatant of each group was collected and transferred to the 96-well plate, and the absorbance at 540 nm of the samples of each group was detected by enzyme labeling instrument. The higher the absorbance of the supernatant, the more blood cells were dissolved, indicating poor hemostatic performance.

Blood Clotting Index (BCI) is an important index used to evaluate the ability of blood to clot, which was calculated as follows:

$$BCI(\%) = A_s/A_b \times 100 \quad (1)$$

where the absorbances of the samples (A_s) and blank control (A_b) were measured at 540 nm, respectively. Here, the mixture of a volume of 100 μL whole blood and 5 mL ultrapure water was served as the blank control.

Whole blood clotting time

Weigh 10 mg samples and put them into the 1.5 mL centrifuge tube. Then 100 μL of whole blood and 10 μL of $CaCl_2$ (0.2 M) solution were added successively. Subsequently, the centrifuge tube was placed in a 37 ℃ water bath and then tilted every 5 s to observe the blood flow status. When the blood stopped flowing, it was recorded as the end time, and the time difference was taken as the coagulation time. The experiment was repeated three times.

Clinical standard blood coagulation tests

The activated partial thromboplastin time (APTT), prothrombin time (PT), thrombin time (TT), and fibrinogen (FIB) tetrameter tests were commonly used to

View Article Online
DOI: 10.1039/D5LC00274E

reflect the coagulation activity clinically. Here, 50 μL of various samples were taken and added into 1.5 mL centrifuge tube (vortex mixing before adding), PPP 500 μL was taken with pipette and added into the sample tube, and PRP was evenly mixed with the sample with gun tip, and incubated at 37 ºC with horizontal oscillation for 15 min. 0.5 mL PPP was added to 50 μL PBS as a blank control and incubated with horizontal oscillations at 37 ºC for 15 min. Three parallel sets were set for both the sample group and the control group. 3, incubation, after the completion of the sample under the centrifugal force 2000 g centrifuge for 10 min, samples from the upper PPP, fully automatic blood coagulation analyzer tests after incubation of the PPP APTT, PT, TT, Fib Numbers. The tests were performed by using an automatic coagulation analyzer (STA R Max, Stago).

Morphology of adherent red blood cells

Firstly, the fresh whole blood was centrifuged at 1500 rpm for 10 min to obtain the red blood cells, and a blood cell suspension was obtained by diluting blood cells using PBS at a ratio of 1:10 before use. Then, 5 mg samples were soaked into 200 μL of diluted whole blood solution and incubated at 37 ◦C for 1 h. Finally, the non-adherent red blood cells were completely removed with PBS for three times. Subsequently, the samples with aggregated red blood cells were fixed with 2.5 % of glutaraldehyde for 2 h. The dehydrated samples were characterized by SEM.

Platelet activation and aggregation analysis

The activated and aggregated platelets on the sample's surface were evaluated by FITC-Phalloidin staining. Initially, 5 mg of the sample was incubated with 200 μL of platelet-rich plasma (PRP) at 37 ◦C for 1 h, then the materials were washed with PBS (pH = 7.4), platelet-poor plasma (PPP) with Kaolinite were served as the negative control. The platelets on the material were fixed with 4 vol% of paraformaldehydes for 20 min. After that, the samples were washed with PBS followed by adding 0.5 mL of 0.1 % Triton X-100, and the Triton X-100 solution was washed away after 5 min using PBS for three times again. Afterwards, 200 μL of 100 nmol/L FITC-Phalloidin (Yeasen Biotechnology Co., Ltd., Shanghai, China) was applied for staining, and the culture plate was put in the dark for 30 min at room temperature. Finally, it was washed with

View Article Online
DOI: 10.1039/D5LC00274E

PBS for 3 times and observed by inverted fluorescence microscope.

To quantify platelets activation, the fresh PRP was obtained for the flow cytometry (FCM) assay. A 10 μL volume of sample suspension (sample in PBS with a concentration of 10 mg/mL) was mixed with 90 μL of PRP for 5 min. Next, 5 μL of the treated blood was stained with platelet-activation-dependent monoclonal antibodies (FITC anti-rat CD61 for platelet activation, PE anti-rat CD62p for activation identification purchased from BD Biosciences) and incubated at room temperature for 20 min avoiding from light. Finally, a flow cytometer was employed to analyze the data. Experiments were performed on three different blood samples.

***In-vivo* hemostatic tests**

All animal procedures were performed in accordance with the Guidelines for Care and Use of Laboratory Animals of "the National Institutes of Health (NIH) of the USA" and approved by the Animal Ethics Committee of "Hubei Provincial Center for Disease Control and Prevention Institutional Animal Care and Use Committee" (Approval number: Number 202529025). The hemostatic test of kaolinite was evaluated using the mouse liver hemorrhage model. Firstly, the mice were anesthetized, and the liver was exposed through an abdominal incision. After carefully removing the tissue fluid surrounding the liver, a pre-weighed filter paper was placed further below the liver. Hepatic hemorrhage was induced with scissors and then immediately overlay different samples on the bleeding site. Data on blood loss and time to hemostasis were recorded throughout the hemostasis process.

Author contributions

Guangyao Li: Writing-original draft, Methodology, Project administration, Investigation, Formal analysis, Data curation. **Liang Wan:** Writing-original draft, Methodology, Investigation, Formal analysis. **Ying Chen:** Writing-review & editing, Supervision, Funding acquisition, Conceptualization. **Xuming Zhang:** Writing-review & editing, Supervision, Funding acquisition, Conceptualization. **Aidong Tang:** Methodology, Resources, Supervision. **Huaming Yang:** Writing-review & editing, Supervision, Funding acquisition, Conceptualization.

View Article Online
DOI: 10.1039/D5LC00274E

Conflicts of interest

There are no conflicts to declare.

Acknowledgments

This work was supported by the National Key R&D Program of China (2023YFE0202600), the CUG Scholar Scientific Research Funds at China University of Geosciences (Wuhan) (2019152), the National Science Fund for Distinguished Young Scholars (51225403) and the Innovation and Technology Commission (ITC) of Hong Kong (ITF-MHKJFS MHP/085/22).

View Article Online
DOI: 10.1039/D5LC00274E

References

[1] J.J. Green, J.H. Elisseeff, *Nature* **2016**, *540*, 386-394.

[2] X.F. Li, P.P. Lu, H.R. Jia, G.F. Li, B.F. Zhu, X. Wang, F.G. Wu, *Coordination Chemistry Reviews* **2023**, *475*, 1-55.

[3] Y. Tan, Q. Yang, M. Zheng, M.T. Sarwar, H.M. Yang, *Advanced Healthcare Materials* **2024**, *13*, 2302700.

[4] Y. Feng, Y.Q. He, X.Y. Lin, M.Y. Xie, M.X. Liu, Y.R. Lvov, *Advanced Healthcare Materials* **2023**, *12*, 2202265.

[5] X.M. Wang, Y.F. Yang, F.F. Yang, B. Mu, A.Q. Wang, *Biomaterials Advances* **2024**, *162*, 213932.

[6] F. Garcia-Villen, I.M.S. Souza, R.D. Barbosa, A. Borrego-Sanchez, R. Sanchez-Espejo, S. Ojeda-Riascos, C.V. Iborra, *Current Pharmaceutical Design* **2020**, *26*, 621-641.

[7] P.K.T. Ngo, D.N. Nguyen, H.P. Nguyen, T.H.H. Tran, Q.N.D. Nguyen, C.H. Luu, T.H. Phan, P.K. Le, V.H.G. Phan, H.T. Ta, T. Thambi, *International Journal Of Biological Macromolecules* **2024**, *279*, 135329.

[8] W. Sajjad, T. Khan, M. Ul-Islam, R. Khan, Z. Hussain, A. Khalid, F. Wahid, *Carbohydrate Polymers* **2019**, *206*, 548-556.

[9] M.V. Serban, S.R. Nazarie, S. Dinescu, I.C. Radu, C. Zaharia, E.A. Istratoiu, E. Tanasa, H. Herman, S. Gharbia, C. Balta, A. Hermenean, M. Costache, *Nanomaterials* **2022**, *12*, 503.

[10] L.S. Yu, X.Q. Shang, H. Chen, L.P. Xiao, Y.H. Zhu, J. Fan, *Nature Communications* **2019**, *10*, 1932.

[11] Y.W. Yang, H. Zhang, F.W. Zeng, Q.Q. Jia, L.N. Zhang, A.X. Yu, B. Duan, *Composites Part B-Engineering* **2022**, *234*, 109661.

[12] M. Long, Y. Zhang, P. Huang, S. Chang, Y.H. Hu, Q. Yang, L.F. Mao, H.M. Yang, *Advanced Functional Materials* **2018**, *28*, 1704452.

[13] M. Long, B. Zhang, S.Y. Peng, J. Liao, Y. Zhang, J. Wang, M. Wang, B. Qin, J.F. Huang, J. Huang, X.P. Chen, H.M. Yang, *Materials Science And Engineering C-Materials for Biological Applications* **2019**, *105*, 110081.

[14] Q.W. Wu, J. Liao, H.M. Yang, *Advanced Science* **2023**, *10*, 2300672.

[15] H. Zadvernyuk, V. Kadoshnikov, S. Shekhunova, S. Remez, *Applied Clay Science* **2021**, *213*, 106236.

[16] Y.J. Yang, M. Jaber, L.J. Michot, B. Rigaud, P. Walter, L. Laporte, K.A. Zhang, Q.F. Liu, *Applied Clay Science* **2023**, *232*, 106801.

[17] M. Miyamoto, S. Sasakawa, T. Ozawa, H. Kawaguchi, Y. Ohtsuka, *Biomaterials* **1990**, *11*, 385-388.

[18] Q. Li, E.L. Hu, K. Yu, R.Q. Xie, F. Lu, B.T. Lu, R. Bao, T.F. Zhao, F.Y. Dai, G.Q. Lan, *Advanced Functional Materials* **2020**, *30*, 2004153.

[19] L. Zhang, Y.X. Sun, L. Peng, W.Z. Fang, Q. Huang, J. Zhang, Z.Y. Zhang, H. Li, Y.J. Liu, Y.B. Ying, Y.C. Fu, *Advanced Science* **2023**, *10*, 2204702.

[20] V.G. Nielsen, T.D. Ward, P.M. Ford, *Journal Of Thrombosis And Thrombolysis* **2018**, *46*, 359-364.

[21] J.S. Li, W. Zhang, L. Lang, C.X. Dong, K. Huang, *Journal Of Cleaner Production*

View Article Online
DOI: 10.1039/D5LC00274E

2024, *441*, 140992.

[22] Y.B. Yuan, X.Y. Tang, J.K. Shi, C.S. Zhou, L.J. Li, H.H. Sun, D.O. Northwood, K.E. Waters, H. Ma, *Molecules* **2024**, *29*, 4129.

[23] Y.Y. Liu, H.J. Yang, L.Q. Sun, J.J. Yuan, K.J. Wan, Z.Y. Miao, Q.G. Xiao, T. Qi, *Journal Of Sustainable Metallurgy* **2024**, *10*, 1580-1593.

[24] Q. Qiao, Y.N. Ding, S.P. Zhao, L. Li, J.L. Liu, X.M. Ren, *Inorganic Chemistry Frontiers* **2017**, *4*, 1405-1412.

[25] Z.P. Shi, Z.H. Yang, Z.D. Wang, L.Y. Liu, *Separation And Purification Technology* **2024**, *332*, 125773.

[26] X. Yu, S.F. Wang, Y. Li, M. Xue, L. Gu, Q.Y. Wu, *Separation And Purification Technology* **2025**, *354*, 129332.

[27] K.P. Galvin, A.M. Callen, S. Spear, *Minerals Engineering* **2010**, *23*, 339-349.

[28] J.F. He, C.G. Liu, P. Hong, Y.K. Yao, Z.F. Luo, L.L. Zhao, *Powder Technology* **2019**, *342*, 348-355.

[29] W.X. Zhao, P. Yin, Z.L. Wang, J.N. Huang, Y.M. Fu, W.J.H. Hu, *Advances In Colloid And Interface Science* **2024**, *334*, 103330.

[30] H.L. Zhang, Y.L. Zheng, S.W. Yu, W.X. Chen, J. Yang, *Nanomaterials* **2022**, *12*, 2103.

[31] M.T.P. Dinh, A. Mukhamedshin, K. Abhishek, F.W. Lam, S.C. Gifford, S.S. Shevkoplyas, *Lab on a Chip* **2024**, *24*, 913-923.

[32] K.C.M. Lee, B.M.F. Chung, D.M.D. Siu, S.C.K. Ho, D.K.H. Ng, K.K. Tsia, *Lab on a Chip* **2024**, *24*, 4182-4197.

[33] K. Abhishek, A. Titus, M.T.P. Dinh, A. Mukhamedshin, C. Mohan, S.C. Gifford, S.S. Shevkoplyas, *Lab on a Chip* **2023**, *23*, 1804-1815.

[34] J.K.S. Tan, S.Y. Park, H.L. Leo, S. Kim, *Ieee Transactions on Biomedical Circuits And Systems* **2017**, *11*, 1431-1437.

[35] X.L. Qiu, J.A. Lombardo, T.M. Westerhof, M. Pennell, A. Ng, H. Alshetaiwi, B.M. Luna, E.L. Nelson, K. Kessenbrock, E.E. Hui, J.B. Haun, *Lab on a Chip* **2018**, *18*, 2776-2786.

[36] X.Y. Liu, J.W. Li, W.C. Zhang, Y.Y. Wang, X.B. Min, Z.H. Yang, M.Q. Shi, Q.W. Wang, X. Yan, L.Y. Chai, *Chemical Engineering Journal* **2024**, *500*, 157509.

[37] O.Y. Golubeva, Y.A. Alikina, E.Y. Brazovskaya, N.M. Vasilenko, *Chemengineering* **2022**, *6*, 78.

View Article Online
DOI: 10.1039/D5LC00274E

Data Availability Statement

This work is original and has not been published previously by any of the authors and/or is not under consideration for publication in another journal at the time of submission. It is agreed to the submission by all the authors. The data that support the findings of this study are available from the corresponding author upon reasonable request.